Research Article Vol. 32, No. 3 / 29 Jan 2024 / Optics Express 3946

Optics EXPRESS

Large transmittance contrast via 90-degree sharp bends in square lattice glide-symmetric photonic crystal waveguides

WEI DAI,[1,2] TAIKI YODA,[1,2] YUTO MORITAKE,[1] AND MASAYA NOTOMI[1,2,3,*]

[1] *Department of Physics, Tokyo Institute of Technology, 2-12-1 Ookayama, Meguro-ku, Tokyo 152-8550, Japan*
[2] *NTT Basic Research Laboratories, NTT Corporation, 3-1 Moriosato-Wakamiya, Atsugi, 243-0198, Japan*
[3] *Nanophotonics Center, NTT Corporation, 3-1 Moriosato-Wakamiya, Atsugi, 243-0198, Japan*
[*] *notomi@phys.titech.ac.jp*

Abstract: We demonstrate an intriguing transmittance contrast in a glide-symmetric square-lattice photonic crystal waveguide with a 90-degree sharp bend. The glide-symmetry gives rise to a degeneracy point in the band structure and separates a high-frequency and a low-frequency band. Previously, a similar large transmittance contrast between these two bands has been observed in glide-symmetric triangular- or honeycomb-lattice photonic crystals without inversion symmetry, and this phenomenon has been attributed to the valley-photonic effect. In this study, we demonstrate the first example of this phenomenon in square-lattice photonic crystals, which do not possess the valley effect. Our result sheds new light onto unexplored properties of glide-symmetric waveguides. We show that this phenomenon is related to the spatial distribution of circular polarization singularities in glide-symmetric waveguides. This work expands the possible designs of low-loss photonic circuits and provides a new understanding of light transmission via sharp bends in photonic crystal waveguides.

© 2024 Optica Publishing Group under the terms of the Optica Open Access Publishing Agreement

1. Introduction

Integrated nanophotonics is expected to play a key role in putting photonics into a chip to overcome the limitation of current CMOS circuits, and to realize high-speed and energy-efficient information and communication technology. The photonic crystal (PhC) attracts much attention because it enables ultrasmall energy-efficient integrable devices with low loss. One important issue of nanophotonics-based integrated circuits is the waveguide bending loss, which becomes serious when the size of waveguides is comparable to the wavelength of light. Although the reflection loss at sharp bends can be reduced in a certain wavelength range by sophisticatedly modifying the bending corners [1–6], it is generally difficult to achieve high transmittance via sharp bends in sufficiently wide wavelengths.

Recently, a number of reports have demonstrated that a variety of valley-photonic crystals (VPhC), a type of photonic topological insulator, support interface states that show high transmittance through 120-degree sharp bends in a wide wavelength range without any sophisticated modification [7–19]. VPhCs are created by breaking the inversion symmetry of honeycomb or triangular lattice PhCs, which gives rise to a binary valley degree of freedom at K and K' points in the wavevector space characterized by the valley Chern number. VPhC waveguides (VPhCWGs) are constructed by connecting two VPhC domains with different valley Chern numbers. Theoretically, it was pointed out that the backscattering would be suppressed in VPhCWGs because of their topological nature, and the high bend-transmittance was attributed to this effect. Such unique properties of VPhCWGs are currently studied in various directions

#513685
Journal © 2024
https://doi.org/10.1364/OE.513685
Received 17 Nov 2023; revised 28 Dec 2023; accepted 3 Jan 2024; published 22 Jan 2024

including ultrahigh-Q nanocavities [7,20–23], compact lasers [21–23], and large-scale broadband photonic routing circuits [10,24].

Another interest of this work is the glide-symmetry. Glide-symmetric waveguides demonstrate novel properties such as enhanced local chirality even in topologically trivial line-defect PhCWGs [25]. Glide-symmetry is also utilized to design cost-effective holey waveguides in microwave region [26,27]. As one of the intriguing natures of VPhCWGs, the bearded type of VPhCWGs which have glide-symmetry at the interface shows a drastic contrast in the bend-transmittance at certain wavelengths. Generally, glide-symmetric waveguides have a symmetry-protected degeneracy point at the Brillouin zone boundary. It was found that the bend-transmittance of glide-symmetric VPhCWGs changes drastically across this degeneracy point [16–18]. In these reports, this novel transmittance contrast is attributed to different band topologies. However, this speculation has not been verified in a rigorous manner.

Although the backscattering of VPhCWGs should be suppressed if the intervalley scattering is prohibited, it is unclear whether the intervalley scattering can be really prohibited in VPhCWGs. In fact, it was suggested that the backscattering in disordered VPhCWGs is not suppressed in conventional situations both experimentally and theoretically [28,29], except in the ultraslow light region. Related to this issue, we have recently discovered that high bend-transmission can be achieved in triangular lattice PhCWGs even without breaking the bulk inversion symmetry [30]. Furthermore, the large bend loss contrast is observed when the inversion-symmetric PhCWGs possess the same glide-symmetric interface as the bearded interface VPhCWGs. Since valley-photonics requires the breaking of inversion symmetry, this suggests that the high bend-transmission and large transmission contrast may have a different origin other than conventional valley-photonics. Indeed, we found that the high bend-transmission is related to the position of circularly-polarized topological singular points. This finding indicates that these phenomena may occur in a wide range of PhCWGs. However, the observations of such interesting bend-transmission have been so far limited to triangular and honeycomb lattice structures, and little attention has been paid to square lattice structures.

In this paper, we demonstrate that similar exotic bend-transmission can be realized in glide-symmetric square-lattice PhCWGs. Note that a square lattice generally does not exhibit the valley-photonic effect, since the valley effect originates from chiral K, K' points in triangular and honeycomb lattices. Here we design 90-degree bends in glide-symmetric waveguides in square-lattice PhCs with the inversion symmetry. We have numerically observed high bend-transmittance and a large transmission contrast between the two waveguide bands above and below the glide-symmetry-induced degeneracy point. We have also confirmed a strong correlation between the bend-transmission and the distribution of circular polarization singularities. All the present results reproduce the interesting properties of the bend-transmission in VPhCWGs, which indicates that these phenomena do not originate from the conventional valley-photonic effect. Furthermore, our results demonstrate that the intriguing high bend-transmission phenomenon can be realized in a wider range of photonic crystal structures, not limited to VPhCs or trivial triangular lattice PhCs. Our results have also provided important intuition in understanding the large transmission contrast that accompanies a glide-symmetric interface.

2. Waveguide design and band structure

In this paper, we theoretically investigate a two-dimensional square lattice PhC constructed with circular silicon rods in transverse-magnetic (TM) polarization, where the electric field is parallel to the rod. The lattice constant a is 500 nm. The radius of silicon rods r is 120 nm. We set the effective refractive index of silicon as $n_{eff} = 2.7$ so that the calculated bandgap approximates that of a three-dimensional structure with a rod height h of 800 nm. As shown in Fig. 1(a), the bulk lattice has a broad TM bandgap at $a/\lambda = 0.328 - 0.420$ (197.1 THz - 251.7 THz). We construct a waveguide along the ΓM direction by removing two rows of silicon rods, thus creating a ΓM-W2WG. As shown in Fig. 1(b), this waveguide has a periodicity $a_w = \sqrt{2}a$. The waveguide possesses glide-symmetry with a glide reflection axis shown as a black dotted line. The horizontal red arrow shows the translation along the waveguide direction for one-half periodicity and the vertical red arrow shows the reflection operation across the axis. The glide-symmetric interface gives rise to a symmetry-protected degeneracy point at $a/\lambda = 0.388$ inside the band gap, separating a low-frequency band (LFB) and a high-frequency band (HFB), as shown in green ($a/\lambda = 0.329 - 0.388$) and yellow ($a/\lambda = 0.388 - 0.420$) background in Fig. 1(c). Two ΓM-W2WGs can be connected by a 90-degree bend without changing their lattice configuration at the interface. It is worth noting that there are two possible types of lattice configuration at the bends. As shown in Fig. 1 (d,e), the mirror-symmetry axis of the 90-degree bend (red dotted lines) either cuts through the centers of the silicon rods (type-A) or lies in between the silicon rods (type-B).

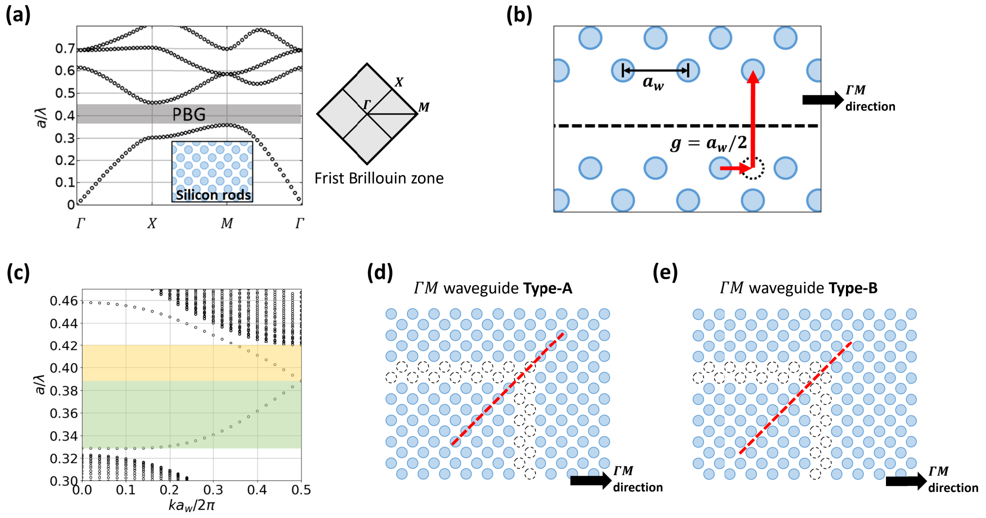

Fig. 1. (a) TM band structure of the bulk photonic crystal. There is a full TM bandgap in $a/\lambda = 0.328 - 0.420$ as shown in the gray box. The inset image shows the bulk square lattice whose ΓM direction is horizontal. The right-side image shows the first Brillouin zone of the square lattice. (b) Mapping of one silicon rod to another via glide reflection. The black dotted line is the reflection axis. The horizontal red arrow shows a translation for half lattice constant. The vertical red arrow shows the mirror reflection. The black arrow shows the ΓM direction. (c) TM band structure of the ΓM-W2WG. There is a degeneracy at $a/\lambda = 0.388$ due to the glide-symmetry. Low-frequency band is marked in green, and the high-frequency band is marked in yellow. There are two types of configurations of the corner lattice in a 90-degree bent ΓM-W2WG. (d) type-A where the mirror-symmetric axis (red dotted line) travels through the rod centers and (e) type-B where the mirror-symmetric axis travels in between the rods.

3. Transmittance via 90-degree sharp bends

Hereafter, we numerically investigate the transmission of the waveguide modes in the straight ΓM-W2WG and type-A and type-B bent ΓM-W2WG. The calculation is conducted using the finite element method (FEM) in COMSOL. We simulate the wave propagation in a rectangular domain with the scattering boundary condition. The wave source is a combination of a surface electric current and a surface magnetic current, set along a line segment (wave source port) perpendicular to the waveguide direction, as shown by the yellow five-stars in Fig. 2 (b,c,e,f).

The port length is $1a$. The surface electric current $\boldsymbol{J_s} = (0, 1, 0)$ and surface magnetic current $\boldsymbol{J_{ms}} = (0, 0, Z_0)$ are applied to the source port, where Z_0 is the impedance of free space. The excited wave is unidirectional, propagating only rightwards when the ratio J_{ms}/J_s is fixed to be Z_0 [31–33]. The bend is located $20a$ away from the wave source. We set three observation line ports perpendicular to the waveguide: port1 port2, and port3 (Fig. 2(c)), each $10a$, $30a$, and $5a$ away from the wave source in both the straight and bent waveguides. The length of the line ports is $4a$. We calculate the transmitted intensity through each observation port as the linear integral of the orthogonal Poynting vector component (power flow) through the port $I = \int_{-2a}^{2a} \boldsymbol{S} \cdot \boldsymbol{e_n}\, dl$. We evaluate the unidirectionality of the excited wave by calculating a loss rate $R_{loss} = \frac{I^{port3}_{str}}{I^{port1}_{str}}$. There are two possible sources of R_{loss}: one is bad coupling between the wave source and the waveguide; the other is weak reflections at the boundaries if the boundary is not perfectly dissipative. The weak reflections may cause Fabry-Perot resonances in the waveguide channels and bring errors to the observed power flow through all ports. Therefore, the power flow calculated at frequencies with a large R_{loss} may not be precise. In frequency range $a/\lambda = 0.340 - 0.420$, R_{loss} is below 0.1 and averages 0.019, indicating that the excited waves are highly unidirectional and possible boundary reflections are low. In the slow-light region $a/\lambda = 0.328 - 0.340$, R_{loss} is above 0.1 and averages 0.162. To keep our evaluation of the transmittance rigorous, we omit the slow-light region $a/\lambda = 0.328 - 0.340$ in the following discussion. We define the transmittance of the straight waveguide as $T_{str} = \frac{I^{port2}_{str}}{I^{port1}_{str}}$ and the transmittance of the bent waveguide as $T_{bend} = \frac{I^{port2}_{bend}}{I^{port1}_{str}}$. This definition is valid as long as the wave is well-confined in the interface and the majority of the power propagates through the observation ports, which is true for the waveguide modes.

Firstly, we investigate the type-A bent ΓM-W2WG. Figure. 2(a) shows the transmittance spectra of the straight (black) and type-A bent (red) ΓM-W2WG. The green and yellow backgrounds show the LFB and HFB regions respectively. The transmittance of the straight waveguide is almost unity at both bands, which serves as a reliable reference for the evaluation of the bent waveguides. Since the calculation errors are large at the slow light region below $a/\lambda = 0.340$, we omit this region and define the LFB to be $a/\lambda = 0.340 - 0.388$. Waveguide modes within this range show high transmittance through a 90-degree bend. The average transmittance $\overline{T_{bend}/T_{str}}$ is 0.90 for LHB. Above the degeneracy point $a/\lambda = 0.388$ starts the HFB. Above $a/\lambda = 0.420$ there appear bulk modes, therefore the range of HFB is $a/\lambda = 0.388 - 0.420$ (yellow region). As shown in the spectrum, the transmittance drops drastically across the degeneracy. The calculated average transmittance of HFB is as low as 0.03, which is significantly smaller than that of LHB. Figure 2(b) shows the E_z distribution at $a/\lambda = 0.37$, where the bend-transmittance is 0.98. One can see that a light wave propagates through the bends without attenuation and no backward-propagating waves are observed behind the wave source. Figure 2(c) shows the E_z distribution at $a/\lambda = 0.39$, where the transmittance is 0.001. One can see that there is no trace of the wave passing through the bend and strong reflected waves are propagating backward behind the wave source.

Next, we investigate the type-B bent ΓM-W2WG. Figure 2(d) shows the transmittance spectra of the straight (black) and type-B bent (red) ΓM-W2WG. Contrary to the result of the type-A bend, there is no apparent contrast in the bend-transmittance between LFB and HFB. The average bend-transmittance is 0.15 in LFB (green region) and 0.37 in HFB (yellow region). Another notable fact is that there is a deep transmittance dip at $a/\lambda = 0.383$ with a transmittance of as low as $4.15E - 4$. Figure 2(e) shows the E_z distribution at $a/\lambda = 0.36$ with a transmittance of 0.20. It can be observed that most of the intensity is reflected at the bend. Figure 2(f) shows the E_z distribution at $a/\lambda = 0.40$ with a transmittance of 0.69. In this case, most of the wave travels through the bend, and a small portion of intensity can be observed behind the wave source.

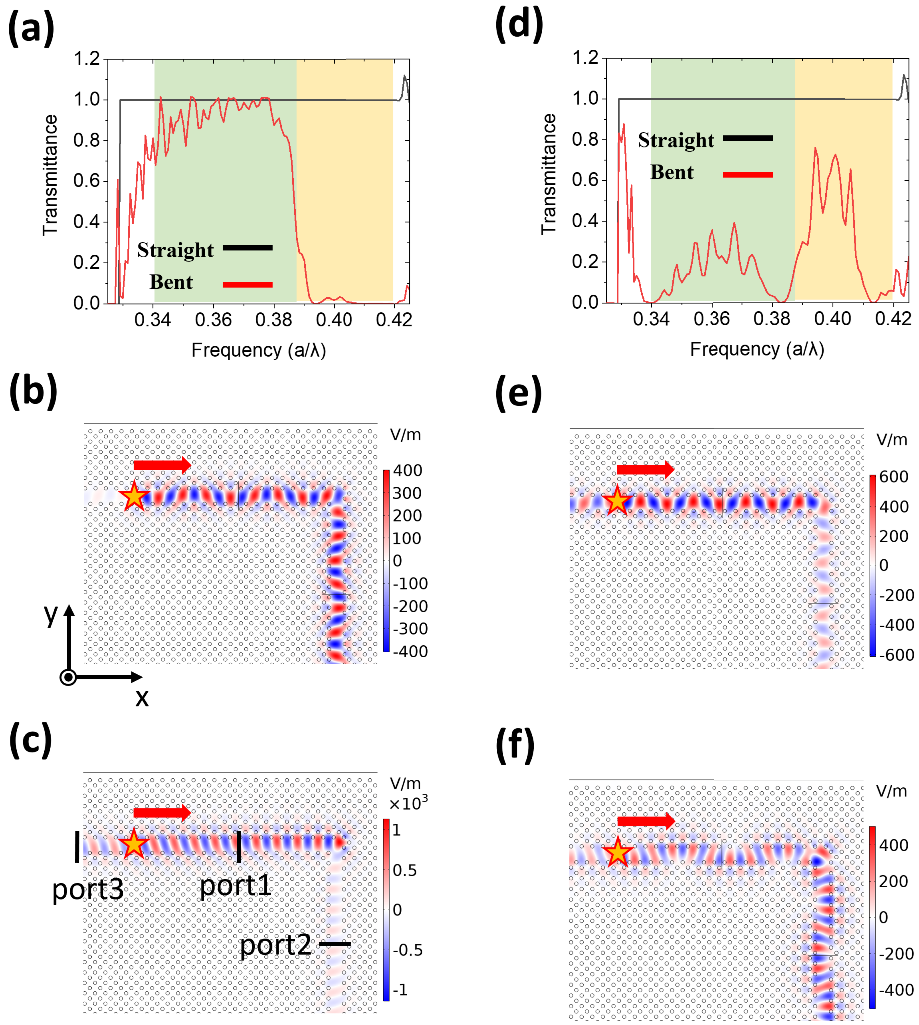

Fig. 2. Simulation results of straight and bent ΓM-W2WGs. (a) Transmittance spectra of the straight (black) and type-A bent (red) ΓM-W2WG. The green and yellow regions show the low- and high-frequency bands respectively. (b,c) E_z distribution at (b) a/λ = 0.37 and (c) a/λ = 0.39 in the type-A bent ΓM-W2WG. Five-stars show the location of wave sources. Red arrows show the direction of excited waves. (d) Transmittance spectra of the straight (black) and type-B bent (red) ΓM-W2WG. (e,f) E_z distribution at (e) a/λ = 0.36 and (f) a/λ = 0.40 in the type-B bent ΓM-W2WG.

Here we summarize the results of simulated transmission. Type-A ΓM-W2WG has high bend-transmission in the LFB and extremely low bend-transmission in the HFB. This phenomenon is very similar to the result observed in valley PhCWGs. In the honeycomb lattice bearded interface valley-PhCWGs reported by Yoshimi et al [16]., and Mehrabad et al. [18], the LFB shows high bend-transmission, and the HFB shows extremely low bend-transmittance via 120-degree bends. On the contrary, the type-B ΓM-W2WG does not show similarities to VPhCWGs or triangular-lattice PhCs. The differences between type-A and type-B ΓM-W2WGs can be explained in the following way. In a 120-degree bend in honeycomb or triangular lattice PhCWG, the mirror-symmetry axis (bisector) of the bend cuts through the lattice sites. In this sense, the symmetry of the type-A bend resembles that of the honeycomb/triangular case. This may explain why type-A shows a very similar bend-transmission to that of triangular- and honeycomb lattices. Naively, if one preserves the mirror-symmetry and the corresponding axis while deforming the square lattice by stretching the lattice grids, it is possible to map the type-A bend to a 120-degree bend in a triangular lattice waveguide. However, preserving the mirror-symmetry in type-B bend inevitably leaves an extra defect along the mirror-symmetry axis, making the type-B bend fundamentally different from the triangular lattice ones.

4. Circular polarization singularities

We have observed a distinctive contrast in the bend-transmission across the degeneracy point in the type-A bent ΓM-W2WG, which is similar to VPhCWGs and some triangular-lattice PhCs. However, the type-B bent ΓM-W2WG does not show such similarity. What causes these differences? In a recent report, we have found that the appearance of high bend-transmittance in a triangular lattice PhCWG is related to the spatial distribution of the circular polarization singularities (CPS) [30]. When the CPSs are near the mirror-symmetry axis of the bend and have strong field intensities, the waveguide tends to have high bend-transmittance. Here, we examine whether the high bend-transmittance condition in the present square lattice PhCWGs is also related to this mechanism. Figure 3 shows a conceptual illustration of the CPS-induced transmittance through 90-degree bends. If the CPSs lie on the mirror-symmetry axis of the bend, the CPSs in the forward propagating wave and the downward propagating wave share the same distribution (Fig. 3(a)). Otherwise, as shown in Fig. 3(b), the CPSs' distribution is reverted in the forward and downward propagating waves, thus not matching each other. A similar mismatch occurs if there are no CPSs (Fig. 3(c)) near the bend. We speculate that the polarization matching would preserve an efficient coupling between different propagation directions and the polarization mismatch would cause corner reflections at the bend. We also assume that polarization matching is effective only when the field intensity is sufficiently strong near the CPSs (bright CPSs).

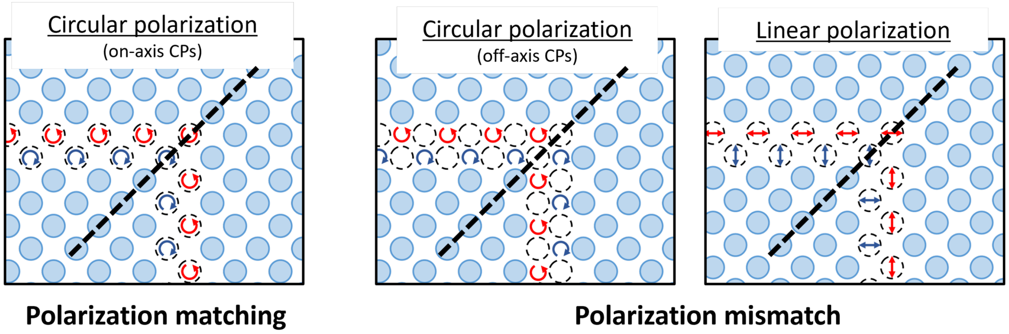

Fig. 3. Schematic illustration of CPS-induced high transmittance via type-A 90-degree sharp bends. Circular arrows represent left- (red) and right- (blue) handed CPSs. Straight arrows represent linear polarizations. The black dotted line indicates the mirror-symmetry axis of type-A bend.

Hereafter, we investigate the CPS distribution of waveguide modes in the LFB (Fig. 4(b-d)) and HFB(Fig. 4(e,f)). We calculate the eigenmode of the ΓM-W2WG unit cell. To identify the locations of CPSs in the ΓM-W2WG, we plot the zero-value isolines of the Stokes parameters [34–37] S_1(red), S_2(green) and S_3(blue). Each plot consists of two unitcells. An illustration of the two-unitcell waveguide is shown in Fig. 4(a). The Stokes parameters of the TM modes are defined as follows:

$$S_1 = |H_x|^2 - |H_y|^2;$$

$$S_2 = 2Re(H_x H_y^*);$$
$$S_3 = -2Im(H_x H_y^*).$$

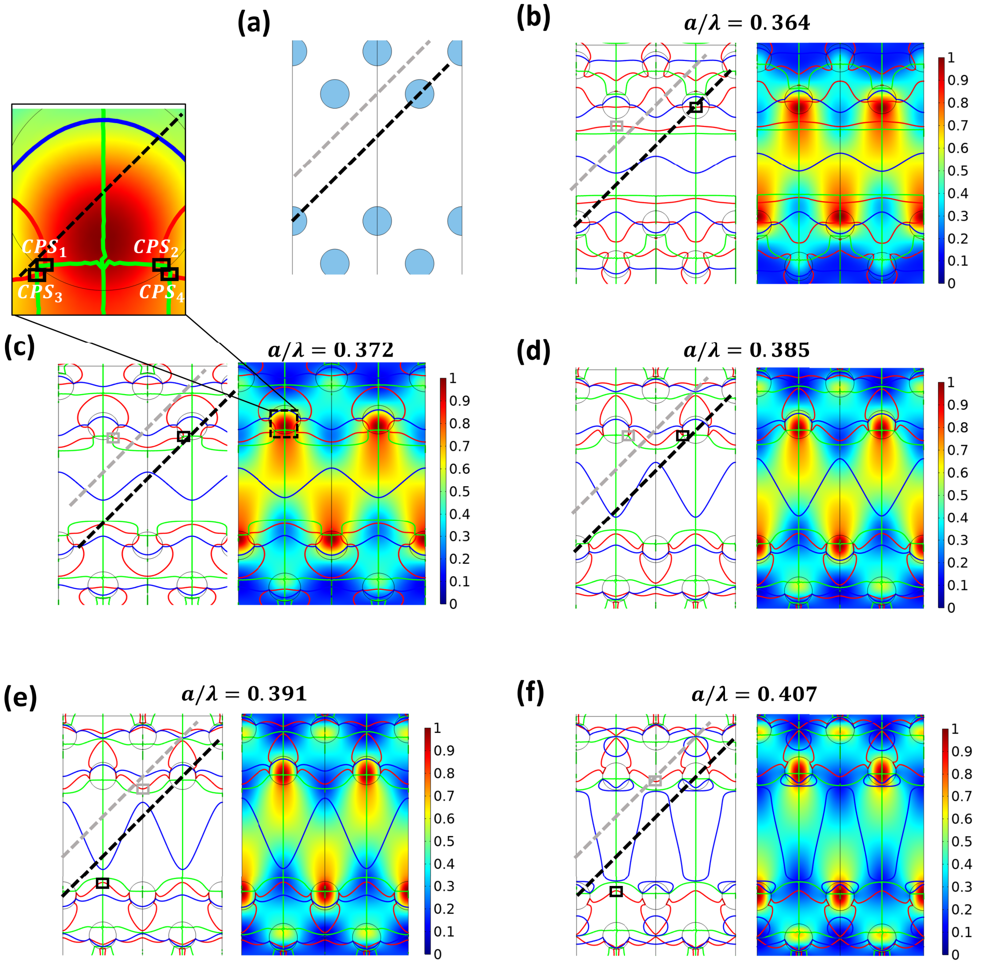

Fig. 4. (a) illustration of two unitcells of the ΓM-W2WG. (b-f) two-unitcell plots of zero-value isolines of Stokes parameters of waveguide modes in LFB (b-d) and HFB (e,f). Black and gray dotted lines indicate the type-A and type-B axis respectively. Black and gray boxes indicate the locations of the nearest CPSs to the type-A and type-B axes respectively. In each sub-figure, the right side plot is the same as the left side, with an additional color map of the normalized magnetic field.

The intersections of red and green curves indicate the position of CPSs. The black and grey dotted lines in Fig. 4 show the mirror-symmetry axis of type-A and type-B bend respectively. The locations of CPSs nearest to the mirror-symmetry axes are marked with black and grey boxes respectively. The right images at each of the panels in Fig. 4(b-f) show the same plot as in the left ones with additional color maps of the normalized magnetic field amplitude $|H|$ (w.r.t. the maximum $|H|$ in the whole unit cell).

Firstly, we investigate the type-A bend. We start from the LFB. At $a/\lambda = 0.364$ (Fig. 4(b)), the transmittance of type-A bent ΓM-W2WGs, $T_A = 1.00$. The distance of the nearest CPS (NCPS, black box) from the type-A axis (black dotted line) in Fig. 4(b) is $D_A^{NCPS} = 0.02a$. The normalized magnetic field amplitude at the NCPS, $|H|_A^{NCPS} = 0.89$. We can see that the NCPS is extremely close to the type-A axis and has an intense magnetic field. At $a/\lambda = 0.372$, there appear four bright CPSs near the silicon rod at the interface, as shown in the enlarged image in Fig. 4(c). CPS1 and CPS2 are inside and CPS3 and CPS4 are outside the silicon rod. The NCPS of type-A axis is CPS1, with $D_A^{NCPS} = 0.03a$ and $|H|_A^{NCPS} = 0.78$. Comparing the T_A at $a/\lambda = 0.364$ and $a/\lambda = 0.372$, we find that T_A drops slightly from 1.00 to 0.95. This can be explained by the fact that at $a/\lambda = 0.372$, D_A^{NCPS} is slightly larger, and $|H|_A^{NCPS}$ is lower. At $a/\lambda = 0.385$ (Fig. 4(d)), D_A^{NCPS} further increases to $0.08a$ and $|H|_A^{NCPS}$ decreases to 0.46, corresponding to the even lower transmittance 0.70 (which, however, is still high compared to those in the HFB).

Now we move on to the HFB. As shown in Fig. 4(e), at $a/\lambda = 0.391$, the $S_1 = 0$ (red) and $S_2 = 0$ (green) isolines diverge near the edge of the silicon rods and the bright CPSs disappear. For the type-A axis, $D_A^{NCPS} = 0.33a$ and $|H|_A^{NCPS} = 0.15$, meaning that there are no bright CPSs near the type-A axis. The type-A bend-transmittance is greatly reduced down to $T_A = 0.11$, much lower than those in the LFB. At $a/\lambda = 0.407$ (Fig. 4(f)), $|H|_A^{NCPS}$ is still 0.15 but the NCPS moves further away from type-A axis. This corresponds to the extremely low T_A of $3.3E - 3$.

We summarize the CPS characteristics of type-A ΓM-W2WGs in terms of T_A, $|H|_A^{NCPS}$, and D_A^{NCPS} for various frequencies in Fig. 5(a-c). The x-axes (frequency) of the three plots are vertically aligned. These three plots visually show a clear correspondence among $|H|_A^{NCPS}$, D_A^{NCPS}, and T_A. One can observe that the waveguide modes in LFB (green) have large magnetic field intensities $|H|_A^{NCPS}$ (Fig. 5(b)), small distances from the type-A axis D_A^{NCPS} (Fig. 5(c)) and thus high bend transmittances T_A (Fig. 5(a)). In contrast, the HFB (yellow) data have small $|H|_A^{NCPS}$ (Fig. 5(b)), large D_A^{NCPS} (Fig. 5(c)) and low T_A (Fig. 5(a)). This clear correspondence in Fig. 5 (a-c) shows that the bend transmittance of type-A samples is dominantly determined by the position of intense CPSs. Note that we recently observed a similar correspondence between the large transmission contrast and the position of CPS in 120-degree sharp bends of the glide-symmetric triangular lattice PhCWGs [30], indicating that both phenomena are governed by the same mechanism.

Next, we analyze the type-B bend in the same manner, focusing on T_B, $|H|_B^{NCPS}$ and D_B^{NCPS}. The type-B axis and the NCPSs are shown in gray dotted lines and boxes in Fig. 4. The summarized results are shown in Fig. 5(d-f). In comparison to the LFB results of the type-A bend(Fig. 5(b)), D_B^{NCPS} is notably large as shown in Fig. 5(f), which explains the relatively low transmittance via the type-B bend. Besides this overall feature, there are several deep transmission dips at $a/\lambda = 0.340$, $a/\lambda = 0.383$, and $a/\lambda = 0.413$ which seemingly cannot be explained by the simple CPS hypothesis. We speculate that this is because the CPS distribution is more complicated in the type-B. In the Appendix, we discuss this issue in more detail and show that these dips may originate from interference, possibly linked to the presence of multiple CPSs.

To summarize, we have confirmed in a wide frequency range that the transmittance of both type-A and type-B bends is dominantly determined by the spatial distribution of the CPSs and field intensities. Smaller distances between CPSs and the mirror-symmetry axis and stronger fields at the CPSs give rise to higher bend-transmittance. This result is consistent with our previous findings for the triangular lattice PhCWGs with 120-degree bends. It is implied that the CPS explanation may be effective for a large class of transport phenomena in PhCWGs, not limited to the structures discussed in this paper and our previous works. Although the characteristics of dips in type-B need further examination (refer to Appendix 1 for more detail), the condition for the high bend transmission in the type-A is well explained by the CPS behavior as visualized in Fig. 5(a-c). As noted before, the type-A axis intersects with silicon rods that generally exhibit large field intensity. In comparison, type-B axis lies in between the silicon rods. Interestingly, bends in triangular-lattice PhCWGs, including valley PhCWGs have a geometrical configuration akin to the type-A bend. This geometrical distinction between type-A and type-B

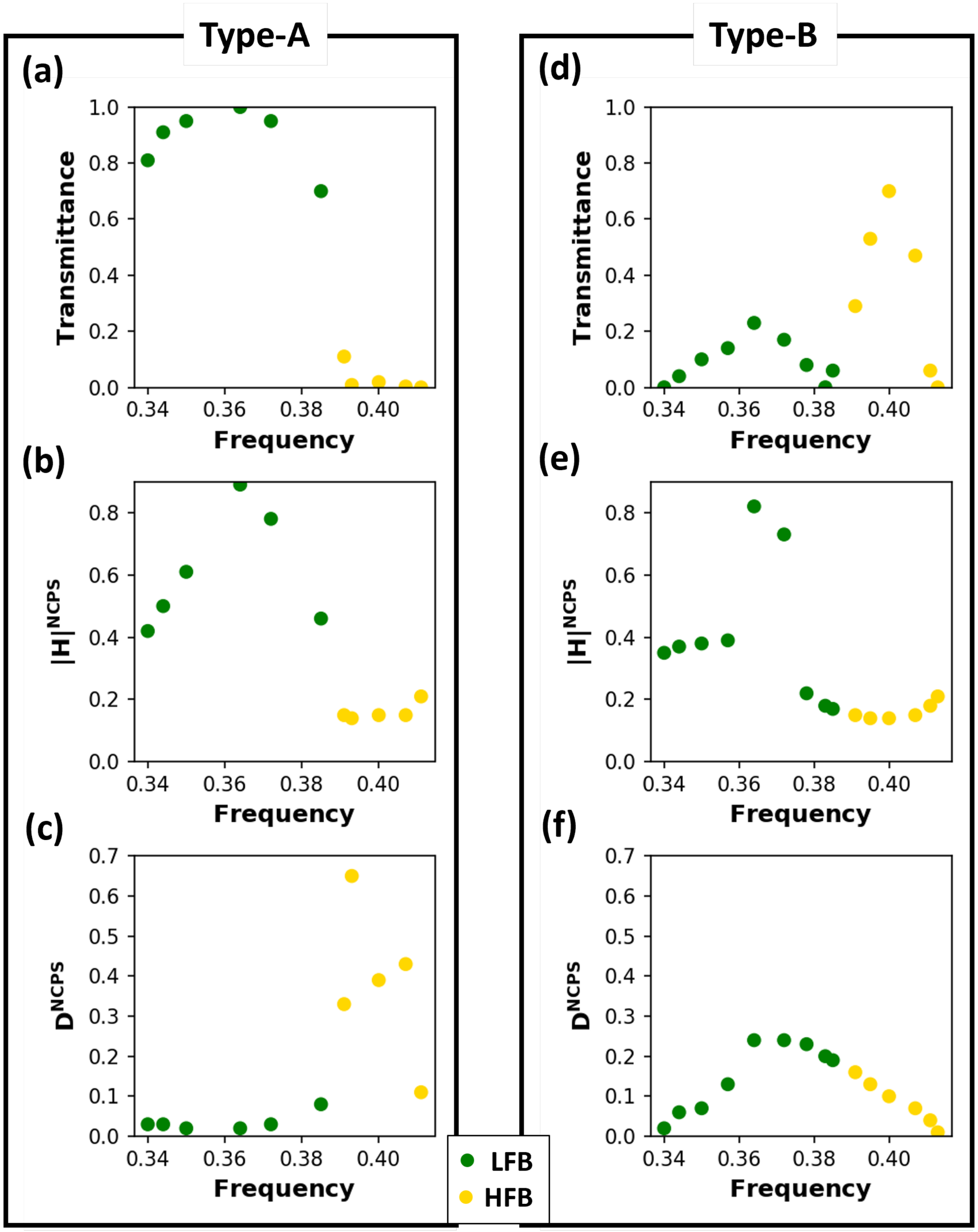

Fig. 5. (a) Bend-transmittance vs. frequency, (b) $|H|^{NCPS}$ vs. frequency and (c) D^{NCPS} vs. frequency plot of the type-A ΓM-W2WG. Green scatters show the low-frequency band data and yellow scatters show the high-frequency band data. (d) Bend-transmittance vs. frequency, (e) $|H|^{NCPS}$ vs. frequency and (f) D^{NCPS} vs. frequency plot of the type-B ΓM-W2WG.

potentially holds significant implications for understanding this phenomenon. We leave this for future study.

5. Conclusion

We have proposed a design for glide-symmetric square-lattice PhCWG by removing two arrays of lattice along the ΓM direction (ΓM-W2WG). In two-dimensional simulations, we have demonstrated extremely high bend-transmittance via a 90-degree bend and a large contrast in transmission properties of the low-frequency band and the high-frequency band. The transmission in type-A bend resembles that of the glide-symmetric bearded-interface Valley-PhCWGs without inversion symmetry, in that the LFB has high transmittance ($T_{ave} = 0.90$) while the HFB has extremely low transmittance ($T_{ave} = 0.03$). This similarity indicates that this large contrast may not be due to the valley-photonic effect, but is specific to glide-symmetric waveguides. In contrast, the type-B bend has middle transmittance at both bands, showing a significant difference from the type-A bend and VPhCWGs, which can be intuitively understood as a direct result of different lattice configurations at the bending corners. A more deliberate analysis demonstrates that the bend-transmittances can be explained by the spatial distribution of the CPSs and field intensities. This finding is consistent with our previous conclusions for the triangular lattice PhCWGs. So far, most previous studies related to this phenomenon have employed honeycomb or triangular lattices because they are directly related to the valley effect, and little attention has been paid to square-lattice PhCs. Our present result thus provides a new perspective in understanding high bend-transmittance in PhCWGs regardless of the lattice configuration and band topology. However, our speculation is preliminary and qualitative. A quantitative derivation of the transmittances remains to be worked out. We also envisage this work to inspire new designs of high-Q nanocavities, orthogonal routing channels, optical switches, and low-loss photonic circuits.

Appendix: transmittance dips in the type-B bend spectrum

As we noted in the main text, there are several deep transmission dips in the spectrum of type-B bend (shown in Fig. 2(d)), which seemingly cannot be explained by the CPS model. Particularly, we observe relatively larger $|H|^{NCPS}$ and smaller D^{NCPS} around dips at $a/\lambda = 0.340$ and $a/\lambda = 0.413$, which according to the CPS model should produce high bend-transmittance instead of extremely low bend-transmittance. Although not conclusive, in this appendix, we conduct a more detailed investigation into the characteristics of transmission dips to draw some possible explanations.

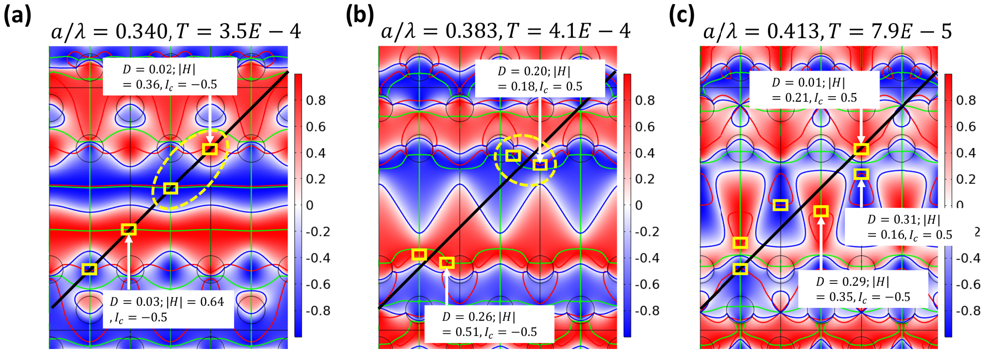

Fig. 6. Zero-value isolines of the Stokes parameters and color maps of $\mathbf{S}_3/\mathbf{S}_0$ at frequencies of the transmittance dips (a) $a/\lambda = 0.340$, (b) $a/\lambda = 0.383$, and (c) $a/\lambda = 0.413$. Multiple CPSs (yellow boxes) exist near the interface with similar distances from the type-B axis (black lines) and magnetic field intensities. The white boxes show the value of distances D, magnetic field intensities $|H|$ and the topological charges I_c

Figure 6 shows the zero-value isolines of Stokes parameters at (a) $a/\lambda = 0.340$, (b) $a/\lambda = 0.383$, and (c) $a/\lambda = 0.413$. The CPSs near the type-B axis (black line) are shown with yellow boxes. We also plot the color maps of the degree of polarization (DoP, calculated as $\mathbf{S}_3/\mathbf{S}_0$). At these frequencies, we find multiple independent CPSs (yellow boxes) having comparable $|H|^{NCPS}$ and D^{NCPS}. These multiple dips have different chirality or topological charges I_c (defined as $I_c = \frac{1}{2\pi}\oint \nabla\phi dl$ where ϕ is the azimuth of the polarization ellipse). The existence of competing multiple CPSs would cause a complicated situation, and this may constitute the reason why it does not lead to high transmittance. For example, the two types of CPSs (enclosed by a dashed yellow circle) in Fig. 6(a) have opposite chirality and the two types of CPSs in Fig. 6(b) have

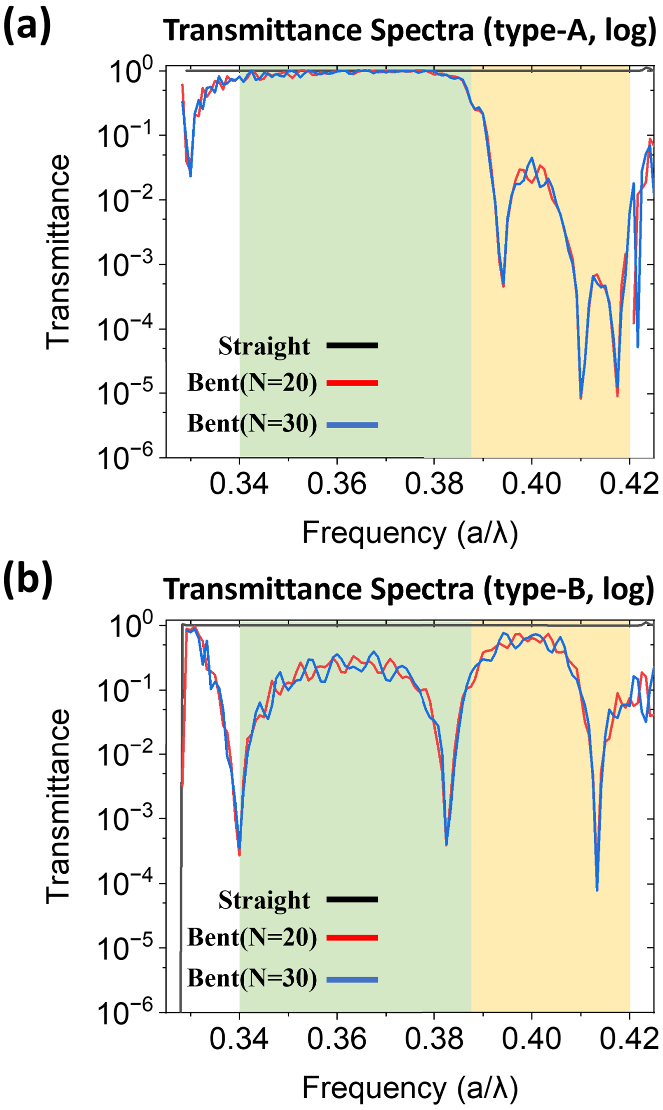

Fig. 7. Transmittance spectra of (a) type-A and (b) type-B ΓM-W2WGs. Red curves show the results of waveguides with port1 and port2 $20a$ away. Blue curves show the results of the waveguide with port1 and port2 $30a$ away, i.e. having longer waveguide length. Black curves show the results of the $N = 20$ straight waveguide.

opposite topological charges. In comparison, away from these dip frequencies, there always exists a single dominant CPS near the type-B axis and thus bend transmittance is relatively high. For example, at $a/\lambda = 0.372$ (Fig. 4(c), gray box) $T_B = 0.17$, and at $a/\lambda = 0.391$ (Fig. 4(e), gray box) $T_B = 0.29$. Therefore, the presence of competing multiple CPSs near the type-B axis may be related to the observed extremely low transmittance in dips.

To clarify the spectral characteristics of dips, we replot the transmission spectra in a logarithmic scale in Fig. 7 of (a) type-A ΓM W2WG and (b) type-B ΓM W2WG. The red and blue curves show the spectra of the same type of bent waveguides with different lengths. Port2 is located Na away from port1 in the waveguide and the waveguide end is fixed to be $10a$ away from port2. Thus, the total waveguide length changes with N. The red curves show the spectra of waveguides with $N = 20$ (the original setting in the main text) and the blue curves show the spectra of waveguides with $N = 30$. Notably, the dips at $a/\lambda = 0.340$, $a/\lambda = 0.388$, and $a/\lambda = 0.413$ in type-B spectra exhibit significant depth that is typical of interference phenomena. Similar deep dips are also found in the low transmission region of type-A spectra. Comparing the red and blue curves for each waveguide type shows that these dips do not depend on the waveguide length. Consequently, these dips cannot be attributed to a simple Fabry-Perot resonance of the waveguide section. We speculate that these dips are caused by local anti-resonance effects at the bending sections, likely due to finite reflection or impedance mismatch. While it is well-known that local resonance can affect bend transmission, such an accidental local resonance effect is inherently narrowband and falls beyond the scope of our study. It's noteworthy that these anti-resonances might result from the interference of multiple competing CPSs and thus the emergence of dips does not contradict the CPS model.

Funding. Japan Science and Technology Agency (JPMJSP2106); Japan Society for the Promotion of Science (JP20H05641).

Acknowledgments. The authors thank Adam Mock for fruitful discussions.

Disclosures. The authors declare no conflicts of interest

Data availability. Data underlying the results presented in this paper are not publicly available at this time but may be obtained from the authors upon reasonable request.

References

1. A. Mekis, J. C. Chen, I. Kurland, *et al.*, "High transmission through sharp bends in photonic crystal waveguides," Phys. Rev. Lett. **77**(18), 3787–3790 (1996).
2. A. Chutinan and S. Noda, "Waveguides and waveguide bends in two-dimensional photonic crystal slabs," Phys. Rev. B **62**(7), 4488–4492 (2000).
3. M. Tokushima, H. Kosaka, A. Tomita, *et al.*, "Lightwave propagation through a 120° sharply bent single-line-defect photonic crystal waveguide," Appl. Phys. Lett. **76**(8), 952–954 (2000).
4. J. S. Jensen and O. Sigmund, "Systematic design of photonic crystal structures using topology optimization: Low-loss waveguide bends," Appl. Phys. Lett. **84**(12), 2022–2024 (2004).
5. J. Yuan, J. Yang, D. Shi, *et al.*, "Design optimization of a low-loss and wide-band sharp 120° waveguide bend in 2d photonic crystals," Opt. Commun. **367**, 356–363 (2016).
6. J. Zhang, J. Yuan, and W. Ai, "Numerical optimization design for waveguide bends with low-loss and wide-bandwidth in two-dimensional photonic crystal slabs," J. Opt. **21**(11), 115103 (2019).
7. J. Ma, X. Xi, and X. Sun, "Topological photonic integrated circuits based on valley kink states," Laser Photonics Rev. **13**(12), 1900087 (2019).
8. T. Yamaguchi, Y. Ota, R. Katsumi, *et al.*, "GaAs valley photonic crystal waveguide with light-emitting inas quantum dots," Appl. Phys. Express **12**(6), 062005 (2019).
9. X.-D. Chen, F.-L. Zhao, M. Chen, *et al.*, "Valley-contrasting physics in all-dielectric photonic crystals: Orbital angular momentum and topological propagation," Phys. Rev. B **96**(2), 020202 (2017).
10. X.-T. He, E.-T. Liang, J.-J. Yuan, *et al.*, "A silicon-on-insulator slab for topological valley transport," Nat. Commun. **10**(1), 872 (2019).
11. X. Wu, Y. Meng, J. Tian, *et al.*, "Direct observation of valley-polarized topological edge states in designer surface plasmon crystals," Nat. Commun. **8**(1), 1304 (2017).
12. Y. Kang, X. Ni, X. Cheng, *et al.*, "Pseudo-spin–valley coupled edge states in a photonic topological insulator," Nat. Commun. **9**(1), 3029 (2018).
13. J. Noh, S. Huang, K. P. Chen, *et al.*, "Observation of photonic topological valley hall edge states," Phys. Rev. Lett. **120**(6), 063902 (2018).

14. A. Kumar, M. Gupta, P. Pitchappa, *et al.*, "Phototunable chip-scale topological photonics: 160 gbps waveguide and demultiplexer for THz 6G communication," Nat. Commun. **13**(1), 5404 (2022).
15. M. I. Shalaev, W. Walasik, A. Tsukernik, *et al.*, "Robust topologically protected transport in photonic crystals at telecommunication wavelengths," Nat. Nanotechnol. **14**, 31-34 (2019).
16. H. Yoshimi, T. Yamaguchi, R. Katsumi, *et al.*, "Experimental demonstration of topological slow light waveguides in valley photonic crystals," Opt. Express **29**(9), 13441–13450 (2021).
17. H. Yoshimi, T. Yamaguchi, Y. Ota, *et al.*, "Slow light waveguides in topological valley photonic crystals," Opt. Lett. **45**(9), 2648–2651 (2020).
18. M. J. Mehrabad, A. P. Foster, R. Dost, *et al.*, "Chiral topological photonics with an embedded quantum emitter," Optica **7**(12), 1690–1696 (2020).
19. Y. Yang, Y. Yamagami, X. Yu, *et al.*, "Terahertz topological photonics for on-chip communication," Nat. Photonics **14**(7), 446–451 (2020).
20. X. Xie, S. Yan, J. Dang, *et al.*, "Topological cavity based on slow-light topological edge mode for broadband purcell enhancement," Phys. Rev. Appl. **16**(1), 014036 (2021).
21. Y. Gong, S. Wong, A. J. Bennett, *et al.*, "Topological insulator laser using valley-hall photonic crystals," ACS Photonics **7**(8), 2089–2097 (2020).
22. Y. Zeng, U. Chattopadhyay, B. Zhu, *et al.*, "Electrically pumped topological laser with valley edge modes," Nature **578**(7794), 246–250 (2020).
23. X. Liu, L. Zhao, D. Zhang, *et al.*, "Topological cavity laser with valley edge states," Opt. Express **30**(4), 4965–4977 (2022).
24. H. Wang, G. Tang, Y. He, *et al.*, "Ultracompact topological photonic switch based on valley-vortex-enhanced high-efficiency phase shift," Light: Sci. Appl. **11**(1), 292 (2022).
25. I. Söllner, S. Mahmoodian, S. L. Hansen, *et al.*, "Deterministic photon–emitter coupling in chiral photonic circuits," Nat. Nanotechnol. **10**(9), 775–778 (2015).
26. M. Ebrahimpouri, O. Quevedo-Teruel, and E. Rajo-Iglesias, "Design guidelines for gap waveguide technology based on glide-symmetric holey structures," IEEE Microw. Wireless Compon. Lett. **27**(6), 542–544 (2017).
27. M. Ebrahimpouri, A. Algaba Brazalez, L. Manholm, *et al.*, "Using glide-symmetric holes to reduce leakage between waveguide flanges," IEEE Microw. Wireless Compon. Lett. **28**(6), 473–475 (2018).
28. G. Arregui, J. Gomis-Bresco, C. M. Sotomayor-Torres, *et al.*, "Quantifying the robustness of topological slow light," Phys. Rev. Lett. **126**(2), 027403 (2021).
29. C. A. Rosiek, G. Arregui, A. Vladimirova, *et al.*, "Observation of strong backscattering in valley-hall photonic topological interface modes," Nat. Photonics **17**(5), 386–392 (2023).
30. W. Dai, T. Yoda, Y. Moritake, *et al.*, "High transmission in 120-degree sharp bends of inversion-symmetric and inversion-asymmetric photonic crystal waveguides," arXiv, arXiv:2310.17487 (2023).
31. M.-C. Tang, H. Wang, and R. W. Ziolkowski, "Design and testing of simple, electrically small, low-profile, huygens source antennas with broadside radiation performance," IEEE Trans. Antennas Propag. **64**(11), 4607–4617 (2016).
32. M. F. Picardi, A. V. Zayats, and F. J. Rodríguez-Fortu no, "Janus and huygens dipoles: Near-field directionality beyond spin-momentum locking," Phys. Rev. Lett. **120**(11), 117402 (2018).
33. Y. Moritake and M. Notomi, "Switchable unidirectional radiation from huygens dipole formed at an exceptional point in non-hermitian plasmonic systems," ACS Photonics **10**(3), 667–672 (2023).
34. G. Arora, Y. Ruchi, and P. Senthilkumaran, "Full poincaré beam with all the stokes vortices," Opt. Lett. **44**(22), 5638–5641 (2019).
35. M. Burresi, R. J. P. Engelen, A. Opheij, *et al.*, "Observation of polarization singularities at the nanoscale," Phys. Rev. Lett. **102**(3), 033902 (2009).
36. B. Lang, D. M. Beggs, A. B. Young, *et al.*, "Stability of polarization singularities in disordered photonic crystal waveguides," Phys. Rev. A **92**(6), 063819 (2015).
37. A. B. Young, A. C. T. Thijssen, D. M. Beggs, *et al.*, "Polarization engineering in photonic crystal waveguides for spin-photon entanglers," Phys. Rev. Lett. **115**(15), 153901 (2015).